# Seeded spin-mixing interferometry with long-time evolution in microwave-dressed sodium spinor Bose-Einstein condensates

# Shan Zhong, Hio Giap Ooi, Sankalp Prajapati, Qimin Zhang, Arne Schwettmann

Center for Quantum Research and Technology, Homer L. Dodge Department of Physics and Astronomy, University of Oklahoma, 440 W. Brooks St., Norman, OK 73019

Abstract. We experimentally demonstrate a new type of spin-mixing interferometry in sodium Bose-Einstein condensates based on seeded initial states. Seeding is useful because it speeds up the generation of entangled pairs, allowing many collisions to take place quickly, creating large populations in the arms of the interferometer. The entangled probe states of our interferometer are generated via spin-exchange collisions in F=1 spinor BECs, where pairs of atoms with the magnetic quantum number  $m_F=0$  collide and change into pairs with  $m_F=\pm 1$ . Our results show that our seeded spin-mixing interferometer beats the standard quantum limit with a metrological gain of 3.69 dB with spin-mixing time t=10 ms in the case of single-sided seeding, and 3.33 dB with spin-mixing time t=8 ms in the case of double sided seeding. The mechanism for beating the standard quantum limit is two-mode spin squeezing generated via spin-exchange collisions. Our results on spin-mixing interferometry with seeded states are useful for future quantum technologies such as quantum-enhanced microwave sensors, and quantum parametric amplifiers based on spin-mixing.

Submitted to: J. Phys. B: At. Mol. Opt. Phys.

### 1. Introduction

Atom interferometry is one of the most precise measurement tools in physics. Several experiments achieved in laboratories have demonstrated that atom interferometers can be excellent in sensing applications [1, 2], cartography mapping [3] and tests of fundamental physics [4, 5, 6]. The performance of an atom interferometer is usually characterized by its sensitivity. For the interferometer prepared in separable states, the attainable sensitivity is fundamentally bounded by the standard quantum limit (SQL)  $\Delta\theta \sim 1/\sqrt{\bar{n}}$  [7], also known as the shot noise limit. However, when interferometers are performed with quantum states where particles are entangled, sensitivities beyond the SQL can be achieved [8]. One fundamental question is understanding which quantum states offer an advantage for quantum metrology. For example, spin-squeezed states for spin 1/2 [9] and spin 1 [10, 11] and some other manybody entangled states such as Greenberger-Horne-Zeilinger (GHZ) are useful for quantum-enhanced metrology [12, 13]. An example of interferometry with entangled states is the SU(1,1) interferometer which is constructed by replacing passive beam splitters in a Mach-Zehnder interferometer with active nonlinear parametric amplifiers [14]. SU(1,1) atom interferometry with spinor Bose-Einstein condensates has been shown to overcome the SQL and gain a sensitivity enhancement compared to its classical counterpart [11, 15, 16, 17, 18].

In a spinor Bose-Einstein condensate (BECs), useful entanglement between particles is generated through spin-exchange collisions [19]. In the three-level F=1 system, the spin-exchange collision is shown in Fig. 1a: the spin-mixing dynamics happen as a pair of  $m_F=0$  atoms couple to  $m_F=1$  and  $m_F=-1$  states after colliding with each other and generate entanglement. The mechanism has been realized as a proof-of-principle SU(1,1) interferometer [20] in a spinor BEC, which is an atomic analog of parametric amplification in optical four-wave mixing [21]. The  $m_F=0$ ,  $m_F=-1$ , and  $m_F=1$  states are analogous to the pump, probe, and conjugate light beams in optical four-wave mixing, respectively.

In this paper, we experimentally investigate the usefulness of seeded initial states for nonlinear interferometry enabled by spin-mixing dynamics (SMD) in F=1 anti-ferromagnetic sodium spinor BECs. We pre-

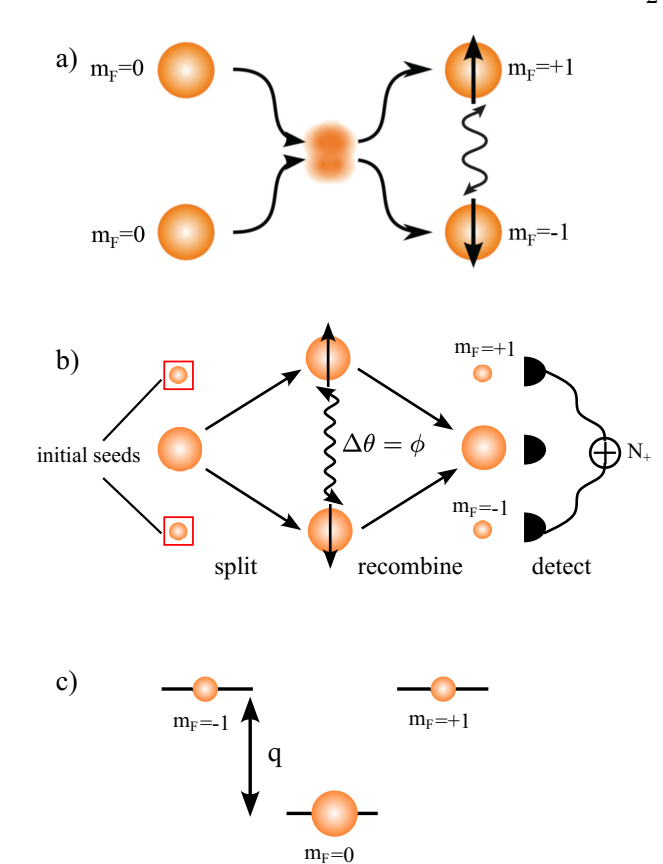


Figure 1. a) Cartoon of a spin-exchange collision in the F=1 ground state. Two atoms with magnetic quantum number  $m_F=0$  can coherently and reversibly scatter into a pair of atoms in the  $m_F=1$  and  $m_F=-1$  states, and vice versa. This creates entanglement as denoted by the wavy line. (b) Cartoon of our seeded spin-mixing interferometer. Shown is an example with a double-seeded initial state. (c) Pair energy diagram showing the effective quadratic Zeeman shift q used to apply quenches and rapid phase shifts.

pare different initial states through either a doublesided seeding or single-sided seeding method. We implement a spin-mixing interferometer that uses seeded states as input, see Fig. 1b. Seeding causes phasesensitive amplification which speeds up the spinmixing, so that a large number of atoms populates the arms of the interferometer [16]. Theoretically, it was found that seeded states can perform better than unseeded states [10]. This suggests that the growth of entanglement is indeed sped up, similar to four-wave mixing with seeded states in nonlinear optics [22]. We use microwave-dressing to control the spin-mixing dynamics and imprint phase-shifts during interferometry, see Fig. 1c. At very long spin evolution time, the interferometer enters into a regime where the interference fringes become highly non-sinusoidal [10, 23]. We investigate the metrological gain for single and double seeded interferometers and different evolution times. For some parameters, we find that the seeded interferometer beats the SQL.

The organization of this paper is as follows. In section two, we work out a theoretical model of spinmixing interferometry. Section three describes our experimental method for initial state preparation of single- and double-sided seeded interferometers and the experimental procedures to realize a seeded spinmixing interferometer. In section four, we present our data on spin-mixing dynamics and interference We compare our data with a theoretical simulation using the truncated Wigner approximation. We calculate our interferometer's sensitivity using the error propagation method. Our data suggest that the sensitivities of our seeded interferometers can reach beyond the SQL, indicating a metrological enhancement of phase sensitivity. Our findings are useful for future quantum technologies, such as quantum-enhanced magnetometers with high spatial resolution, quantum-enhanced microwave sensors, and other future devices based on matter-wave quantum optics in spin space.

# 2. Theory

# 2.1. Theoretical Background of Spin-1 Interferometry

We start by introducing the Hamiltonian and theoretical framework that describes our experiments. We consider an F=1 spinor BEC consisting of N sodium atoms confined in a tight 3D optical trap. In our experiments, the Thomas-Fermi radius of the spinor BEC is smaller than the spin healing length, and the spin-dependent interaction is much weaker than the density-dependent interaction. Hence, we can apply the single-mode approximation (SMA) [24], which assumes all spin components share the same spatial density profile. As a result, the dynamics are governed by the spin-part of the Hamiltonian. In the SMA, the spin-part of the Hamiltonian is [25]:

$$\hat{H} = \frac{c}{N} (\hat{a}_0^{\dagger} \hat{a}_0^{\dagger} \hat{a}_{+1} \hat{a}_{-1} + \hat{a}_{+1}^{\dagger} \hat{a}_{-1}^{\dagger} \hat{a}_0 \hat{a}_0)$$

$$+ \frac{c}{N} (\hat{N}_0 - \frac{1}{2}) (\hat{N}_{+1} + \hat{N}_{-1}) + q(\hat{N}_{+1} + \hat{N}_{-1}).$$
(1)

The first term on the right-hand side is identical to the four-wave mixing term from nonlinear quantum optics [14], which here describes spin-exchange collisions between atoms. The second term refers to an energy shift due to elastic collisions. The last term describes the effective quadratic Zeeman shift. It contributes to the linear phase shift during spin-mixing interferometry and can be used to quench the system. The operators  $\hat{a}_i^{\dagger}$  and  $\hat{a}_i$  satisfy the bosonic commutation relation  $[\hat{a}_i,\hat{a}_j^{\dagger}]=\delta_{ij}$  where  $\hat{a}_i^{\dagger}$  create and  $\hat{a}_i$  destroy an atom in hyperfine state  $|F=1,m_F=i\rangle$ . The number operator for each mode is  $\hat{N}_i$  which is defined as  $\hat{N}_i=\hat{a}_i^{\dagger}\hat{a}_i$ . The coefficient q is the effective quadratic energy shift which can be described as following

$$q = q_B + q_M$$
 (2)  
=  $aB^2h + \frac{1}{2}(\Delta E_{m_F=1} + \Delta E_{m_F=-1} - 2\Delta E_{m_F=0}).$ 

Here,  $q_B$  is the quadratic Zeeman shift due to an applied dc magnetic field, and  $q_m$  is the shift due to an applied ac magnetic field, in our case applied via microwave dressing.  $\Delta E_{m_F}$  is the ac Zeeman shift of a target energy level, which can be approximated as [26, 27]

$$\Delta E_{m_F} = \frac{\hbar}{4} \sum_{k=0,\pm 1} \frac{\Omega_{m_F,m_F+k}^2}{\Delta_{m_F,m_F+k}}$$

$$= \frac{\hbar}{4} \sum_{k=0,\pm 1} \frac{\Omega_{m_F,m_F+k}^2}{\Delta - (g_F m_F - g_{F'}(m_F + k))\mu_B B},$$
(3)

when  $\Omega \ll \Delta$ , as in our experiments. Here  $m_F$  is the magnetic quantum number in the F=1 manifold, which takes values -1,0, and 1. k takes the value of -1, 0, and 1 such that  $m_F+k$  defines the magnetic sublevels in the F=2 manifold. We define  $\Delta_{m_F,m_F+k}=\Delta-(g_Fm_F-g_{F'}(m_F+k))\mu_BB$  as the frequency detuning of the microwave pulse with respect to the  $|F=1,m_F\rangle \rightarrow |F=2,m_F+k\rangle$  transition, where  $g_{F,F'}=\pm 1/2$ .  $\Omega_{m_F,m_F+k}$  is the on-resonance Rabi frequency between  $m_F$  and  $m_F+k$  states, which can be directly obtained from experiments or calculated using Clebsch-Gordan coefficients.

In Eq. 1, c is the spin-dependent interaction parameter,  $c=c_2\bar{n}$ . It is determined by the mean spatial number density  $\bar{n}$  and the spin-dependent interaction coefficient  $c_2$  [24]. Sometimes, the undepleted pump approximation (UPA) is applied to simplify  $\hat{H}_{\rm SMD}$  by replacing  $a_0^{\dagger}$  and  $a_0$  with a complex number  $\sqrt{N_0}e^{-i\phi_0}$ , which reduces Eq. 1 to a form in terms of the SU(1,1) operators [28]

$$\hat{H}_{\text{UPA}} = \frac{c}{N} (2N_0 \hat{K}_x) + (2\hat{K}_z - 1) \left[ \frac{c}{N} (N_0 - \frac{1}{2}) + q \right]. (4)$$

Here,  $\hat{K}_x$  and  $\hat{K}_y$  are the generators of the SU(1,1) symmetry group.

Physically, the undepleted pump approximation is valid when the majority of the atoms are in the  $m_F = 0$  pump mode. This places restrictions on the initial state and on the evolution time of the interferometers that can be described by the UPA [23].

Our seeded F=1 spin-mixing interferometers are realized in three major blocks, as shown in Fig. 2.

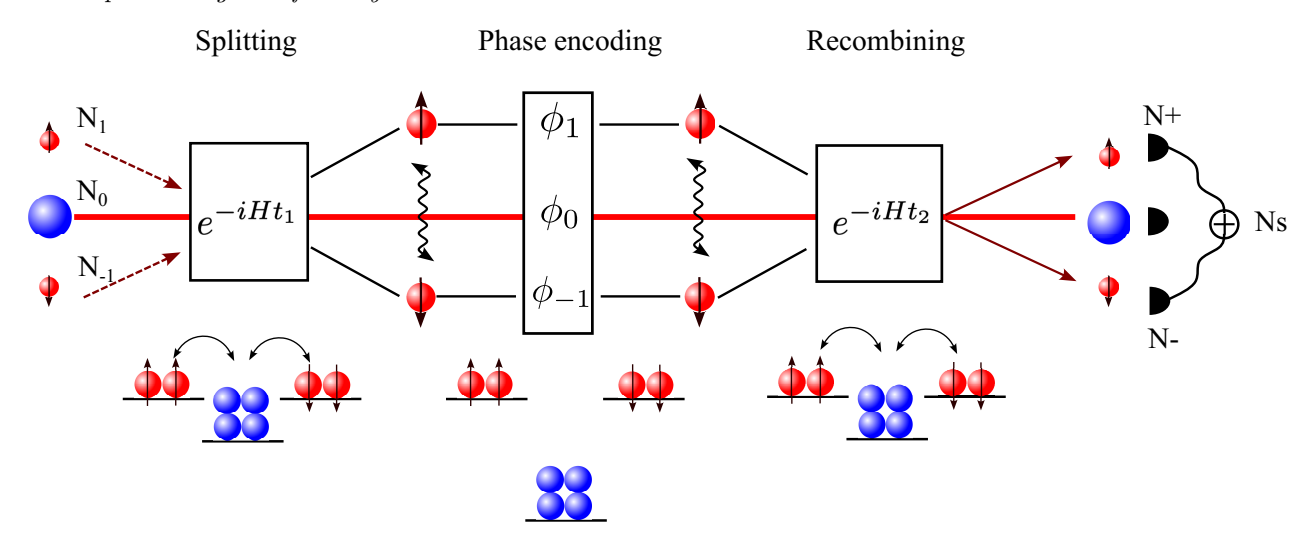


Figure 2. Schematic of our three-mode nonlinear interferometer based on spin-mixing dynamics. The initial state is a pure BEC in the coherent spin state  $|\alpha_{-1}, \alpha_0, \alpha_1\rangle$  with some classical seeds in  $m_F=\pm 1$  states. Here,  $|\alpha_{\pm 1}|^2$  are the mean values of the initial seed numbers, and  $|\alpha_0|^2$  is the mean value of the initial number of  $m_F=0$  atoms. The spin-mixing Hamiltonian H triggers the nonlinear "path" splitting or recombining by creating (annihilating) paired atoms in  $|F=1, m_F=\pm 1\rangle$  components from (into) the  $|F=1, m_F=0\rangle$  state. The phase encoding shifts the spin component  $|1, 0\rangle$  and adds a relative phase  $\phi=2\pi\times 2q\tau$  to the overall spinor phase  $\theta=\theta_1+\theta_{-1}-2\theta_0$ . In the end, the total number of atoms,  $N_s=N_{+1}+N_{-1}$ , in  $|F=1, m_F=\pm 1\rangle$  is measured.

First, we prepare an initial state  $|\Psi(t=0)\rangle$  with some classical seeds in the side modes (the  $|1,\pm 1\rangle$  components) at spin evolution time t=0. After quenching the system by rapidly reducing the ratio |q|/c, the system starts to evolve under the spin-mixing Hamiltonian H for variable time  $t_1$ ,

$$|\Psi(t_1)\rangle = e^{-i\hat{H}t_1/\hbar} |\Psi(t=0)\rangle, \qquad (5)$$

the spin-exchange collisions cause the atoms to change from the  $|1, 0\rangle$  state to  $|1, \pm 1\rangle$  and generate entanglement between them. This step is referred to as "splitting".

Second, the phase imprinting operator is applied to  $|\Psi(t_1)\rangle$  for time  $\tau$  by changing q to a large value  $|q|\gg c$  for a short time compared to h/c,

$$|\Psi(t_1 + \tau)\rangle = e^{-i\hat{H}_{ps}(q)\tau/\hbar} |\Psi(t_1)\rangle \tag{6}$$

the phase imprinting operator  $\hat{H}_p s$  corresponds to the last term in Eq. 1. When  $|q|\gg c$ , the last term of the spin-mixing dynamics Hamiltonian dominate, and the spin-exchange collisions are energetically forbidden. Hence, the phase shift Hamiltonian  $H_{ps}$  is simply

$$\hat{H}_{ps} = q(\hat{N}_{+1} + \hat{N}_{-1}). \tag{7}$$

In this step, the phase encoding shifts the spin component  $|1, 0\rangle$  and adds a relative phase  $\phi = 2\pi \times 2q\tau$  to the overall spinor phase  $\theta = \theta_1 + \theta_{-1} - 2\theta_0$ .

The last step is referred to as "recombining". It is realized by applying an approximate time-reversal dynamics of the splitting process. The entangled probe states become disentangled and traced back approximately to the input state if no additional phase is added. The commonly adopted approach

for realizing time-reversed dynamics comes from time-forward evolution with a sign-flipped Hamiltonian [18]. In the spinor BEC system, an exact time reversal is only possible in the limit of infinitely small evolution times and with a phase imprinting of  $\pi$  [17]. In our case, the phase shift  $\phi$  which is applied during the phase imprinting step consists of both the reversal phase shift and any additional phase. So, after phase imprinting, we apply  $\hat{H}$  again,

$$|\Psi(t_1 + \tau + t_2)\rangle = e^{-i\hat{H}t_2/\hbar} |\Psi(t_1 + \tau)\rangle, \qquad (8)$$

where  $t_2$  is the time for "recombining," which is set equal to  $t_1$  to accomplish approximate time-reversal spin evolution [17]. With the presence of a finite encoding phase, the "recombining" mechanism does not couple the entangled probe state back to the same state as the input state. Instead, it gives rise to a phase-dependent output state. Approximate time-reversal is constrained to short-term spin evolution before the probe states become too deeply entangled to be disentangled. For long-term spin evolution, the described steps realize a nonlinear atom interferometer [18]. After this procedure, the number of atoms in each spin component is measured.

#### 2.2. Phase Estimation

In our experiment, the mean value  $\langle \hat{N}_s \rangle$  and the standard deviation  $\Delta N_s$  after the spin-mixing dynamics of the "splitting" and "recombining" steps are the two important physical quantities to characterize the interferometer performance. Here  $\langle \hat{N}_s \rangle$  is the total number

of atoms in  $|F=1, m_F=\pm 1\rangle$  states. We define

$$\hat{N}_s = \hat{N}_{+1} + \hat{N}_{-1},\tag{9}$$

where  $\langle \hat{N}_s \rangle = \langle \Psi(t) | \hat{N}_s | \Psi(t) \rangle$ , and

$$\Delta N_s = \sqrt{\langle \hat{N}_s^2 \rangle - \langle \hat{N}_s \rangle^2}.$$
 (10)

We analyze  $\langle \hat{N}_s \rangle$  and  $\Delta N_s$  as a function of relative phase  $\phi$  to find operating points with the best sensitivity. The phase sensitivity  $\Delta \phi$  is defined through error propagation [11], and it is evaluated at time  $t = t_1 + \tau + t_2$ ,

$$\Delta \phi = \frac{\Delta N_s(t)}{|\partial N_s(t)/\partial \phi|}.$$
(11)

The phase sensitivity  $\Delta \phi$  is then compared to the lowest possible sensitivity of separable states, which is the standard quantum limit (SQL)  $1/\sqrt{N_s(t_1)}$  here, to show if there is an enhanced gain for the nonlinear interferometer [18, 17].

The lower bound for the error propagation-based sensitivity is set by the quantum Cramér-Rao bound

$$\Delta\phi_{QCR} = \frac{1}{\sqrt{F_Q[|\Psi(t_1)\rangle, \hat{N}_s/2]}},\tag{12}$$

where the quantum Fisher information  $F_Q$  depends on  $|\Psi(t_1)\rangle$  and the linear phase generator  $\hat{N}_s/2$ . We further assume our state is a pure state after the spin-mixing dynamics of the "splitting", then the quantum Cramér-Rao bound is obtained from  $\Delta\phi_{QCR}=1/\Delta N_s(t_1)$ . Ideally, one should use a state which gives maximum  $F_Q$  to optimize the interferometric gain and operate in the regime where the error propagation-based sensitivity  $\Delta\phi$  is as close as possible to the best achievable phase sensitivity. We also compare to the Heisenberg limit  $\Delta\phi_{HL}$  which is defined in terms of the number  $N_s(t_1)$  of atoms at side modes at time  $t_1$ ,

$$\Delta \phi_{HL} \propto \frac{1}{N_s(t_1)}.\tag{13}$$

The Heisenberg limit is the ultimate limit for the phase sensitivity that can be reached in an ideal system with the absence of noise.

#### 3. Experimental Procedures

#### 3.1. Initial State Preparation

We start the experiment by preparing  $\sim 25000$  atoms in a pure sodium BEC in a crossed-beam optical dipole trap via evaporative cooling. Our experimental apparatus has been described in detail in Ref. [29]. The trapping potential near the minimum is approximately harmonic and approximately axially symmetric. The trapping laser beam is far red-detuned, having wavelength  $\lambda = 1064$  nm and a beam waist  $(1/e^2 \text{ radius})$  of  $\sim 26 \ \mu\text{m}$ . The measured trap frequencies are

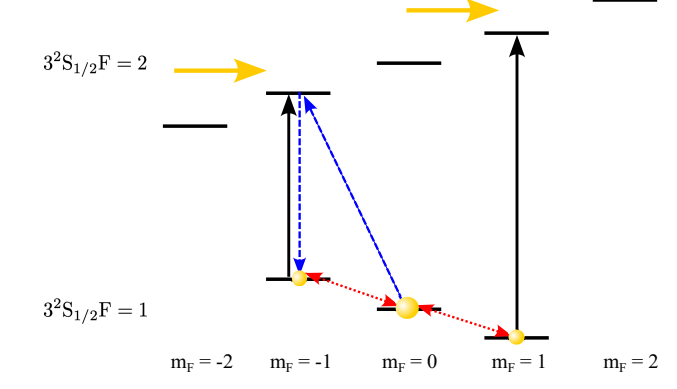


Figure 3. Preparing seeded initial states. After clean-up via microwave sweeps, the single-sided seeding is realized using two consecutive microwave  $\pi$  pulses (blue dash arrows). The double-sided seeding is realized by applying a radio-frequency pulse (red dot arrows) to seed  $|F=1, m_F=\pm 1\rangle$ , simultaneously.

 $(\omega_x, \omega_y, \omega_z) \approx 2\pi \times (123(15), 125(15), 248(10))$  Hz, and the strongest confinement direction z is aligned with the direction of gravity. The uncertainties represent estimated day-to-day fluctuations. A bias magnetic field is fixed at B=0.428(2) G and applied along the z direction to cause a Zeeman splitting of the F=1 hyperfine manifold. The quoted uncertainty in B is determined by applying resonant RF fields, measuring the resulting Rabi oscillations in the F=1 manifold, and fitting the results to a three-level model. The bias magnetic field corresponds to a linear Zeeman shift of  $(300 \text{ kHz}) \times h$  and a quadratic Zeeman shift between  $m_F=0$  and  $m_F=\pm 1$  sublevels of  $(141 \text{ Hz}) \times h$ .

The atomic population fraction in each sublevel can be controlled by applying an empirically determined bias magnetic field at the end of forced evaporation. With this method, we populate most of the atoms into the  $|F=1, m_F=0\rangle$  state before initializing the spin-mixing interferometry experiment. In order to have a pure state of  $|F=1, m_F=0\rangle$  before seeding, atoms in the unwanted states  $|F=1, m_F=\pm 1\rangle$  have to be cleaned. This clean-up step is realized by applying two consecutive one-millisecond long microwave sweeps through the  $\Delta m_F = 0$  resonances, such that the atoms in  $|F=1, m_F=\pm 1\rangle$  states are adiabatically transferred to  $|F=2, m_F=\pm 1\rangle$  states, respectively. Immediately after all unwanted atoms are in the F=2 manifold, we apply a short, 200  $\mu$ s, pulse of on-resonant light which couples the F = 2 and F' = 3states. The resulting absorption gives a momentum kick to the F=2 atoms, causing these unwanted atoms to leave the optical dipole trap. In this way, we prepare  $\sim 21,000$  atoms in the desired state  $|F=1,m_F=0\rangle$ , and all other hyperfine states are empty.

After clean-up, the initial seeded states are prepared independently at the beginning of each interferometry experiment with either single- or double-sided seeding, as illustrated in Fig. 3. For single-sided seeding, a small fraction of the total atom number is coherently transferred to the  $|F=1, m_F=-1\rangle$  state by applying two consecutive microwave pulses. The first pulse transfers some atoms from the  $|F=1, m_F=0\rangle$  state to the intermediate  $|F=2, m_F=-1\rangle$  state. The second pulse is a  $\pi$  pulse that transfers all atoms from the intermediate  $|F=2, m_F=-1\rangle$  state to the final  $|F=1, m_F=-1\rangle$  state. The fraction of the seed is controlled by the power of the first microwave pulse. Using this method, we seed 10% of all the atoms into the  $|F=1, m_F=-1\rangle$  state. All microwave fields in our experiment are applied using our custom versatile microwave source, described in detail in Ref. [29].

For double-sided seeding, instead of using the microwave pulses to prepare the seeding, we apply a short on-resonant rf pulse with a frequency of 300 kHz. The rf pulse is resonant with the linear Zeeman shift between the sublevels in the F = 1 manifold. The rf pulse simultaneously transfers the same atom numbers from the  $|F=1, m_F=0\rangle$  state to both  $|F=1, m_F=-1\rangle$  and  $|F=1, m_F=1\rangle$  states. Here, the quadratic Zeeman shift can be ignored because it is smaller than the pulse bandwidth. The number of seed atoms can be controlled either by changing the duration or the power of the radio frequency pulse. We set the pulse duration and power to transfer 5% of atoms into each side mode, for a total of 10%. This allows us to investigate spin-mixing interferometry with double-sided seeded initial states.

We numerically analyzed the sensitivity as a function of seeding percentage for long evolution times, and found that metrological gain can be achieved for seeds of 0, 2%, 5%, and 10% seeding, but there was no gain at 20% seeds. This numerical analysis was done in Ref. [23]. In light of that study, we expect metrological gain also for lower seeds than 10%, but not for seeds on the order of 20% or higher. We focused on 10% seeding in this manuscript because the seed populations in this case are large enough to be observed accurately with our imaging system, when compared to background noise.

# 3.2. Experimental Interferometry Sequence

After preparing the initial seeded states, the spinmixing interferometry can be experimentally realized in the following three steps: state splitting, phase imprinting, and state recombining.

The state-splitting step is realized by applying the spin-mixing Hamiltonian  $H_{\rm SMD}$  for a time  $t_1$ . We control the spin-mixing dynamics by quenching the  $m_F=0$  energy, as shown in Fig. 4. The detuning of the microwave dressing field is set to  $\Delta=75$  kHz blue shift from the  $|F=1,m_F=0\rangle$  to  $|F=2,m_F=0\rangle$  clock transition. Fig. 4a shows the energy diagram

before the quench: no spin-exchange collisions happen because the population transfer between  $m_F=0$  and  $m_F=\pm 1$  is energetically forbidden. After applying the microwave dressing field (Fig. 4b), the  $m_F=0$  state is quenched close to  $m_F=\pm 1$  states. The value of q depends on the power of the microwave field. Coherent spin population oscillations between the  $m_F=0$  state and  $m_F=\pm 1$  states can now happen after the quench. Their amplitude and period depend on the interplay between the spin-dependent interaction energy c and the effective quadratic Zeeman energy c.

The target value q can be chosen by changing either the magnetic field magnitude or the microwave dressing power. We use microwave dressing for this purpose, because it is more versatile than changing the magnetic field. The microwave power and frequency can be switched on or off or changed almost instantaneously, within a few ns, which is crucial for quenching the system. Magnetic fields require high voltages to switch that fast due to the back-emf generated in the coils. In addition, a fast-changing microwave field doesn't cause the large eddy currents in the stainless steel vacuum chamber that a rapid magnetic field change would cause. With microwave dressing, q can be chosen to be either positive or negative, depending on the sign of the microwave detuning  $\Delta$ . In contrast, a magnetic field only allows for a positive sign of q. Our microwave generator has an output power range from -30 dBm to 42 dBm, which corresponds to a large range of choices for q, spanning over two orders of magnitude.

The phase imprinting step happens at the end of the first spin-mixing dynamics, after evolution time  $t_1$ . We apply a relative phase shift to the system by changing the quadratic Zeeman shift q, such that  $|q|\gg c$ . This is experimentally realized by decreasing the detuning of the microwave field from  $\Delta = 75$  kHz to  $\Delta = 30 \text{ kHz}$  as well as increasing the microwave power. Since our Rabi frequency for coupling  $|F=1, m_F=0\rangle$ to  $|F=2, m_F=0\rangle$  is less than 10 kHz, our detuning is still sufficiently large compared to the Rabi frequency, as verified by the fact that we didn't observe a large atom loss during the experiment. Due to the large ratio of |q|/c during the phase imprinting, population changes are suppressed and only an extra q-dependent spinor phase shift ensues. The relative spinor phase shift induced by the microwave kick is  $\phi \approx -2\pi \times 2q\tau$ , which depends on the effective quadratic Zeeman shift q and the pulse length  $\tau$ . Here we keep  $\tau$  constant for 1 ms and scan the relative phase  $\phi$  by scanning q. The range of q values is from q/h = -100 Hz to q/h = -1040 Hz.

After phase imprinting, the entangled states "recombine" under another  $H_{\rm SMD}$  for time  $t_2$  ( $t_2 = t_1$ ). During this process, the entangled  $m_F = \pm 1$  pairs

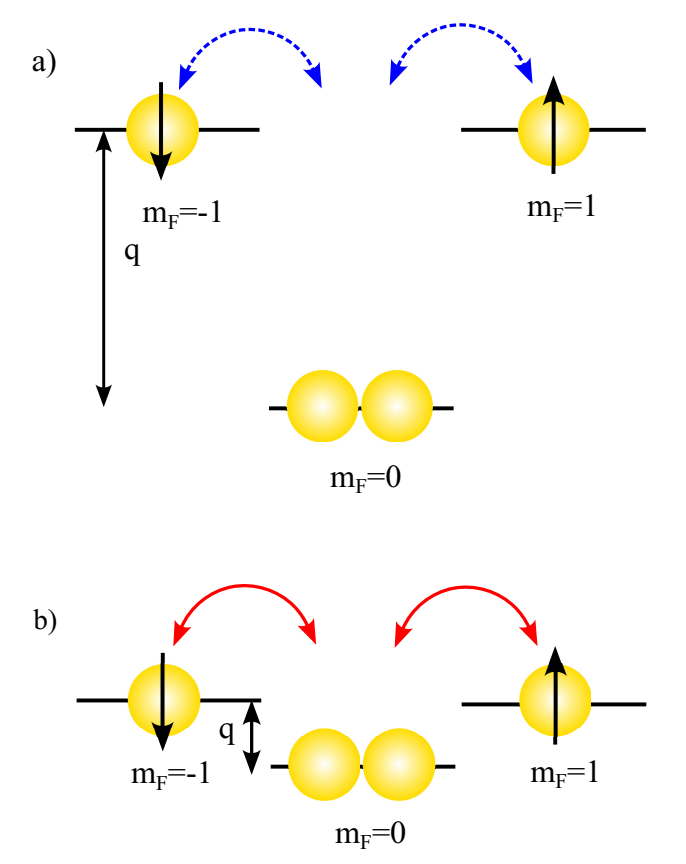


Figure 4. Schematic of a quenching process illustrated with pair energy levels of the  $m_F=0$  and  $m_F=\pm 1$  states with single-particle detuning q. The linear Zeeman shift has been rotated out. The blue dashed arrow means no spin exchange happens, and the solid red arrow means spin exchange can happen. a) before quenching the Hamiltonian, the effective quadratic Zeeman shift q is large, and the spin mixing dynamic is energetically forbidden. b) after quenching, the spin mixing starts, and the competition between the spin-interaction c and q determines the exact dynamics of the spin oscillations.

partially disentangle and transfer back to the  $m_F=0$  state. With different imprinted phases, we can either control the evolution of  $N_s$  to continue evolving or recover back the approximate initial state. After a total time  $t=t_1+\tau+t_2$ , the optical dipole trap is switched off, a 9 ms long Stern-Gerlach pulse is applied, and the false color absorption images are taken to measure the atom number for the three spin components.

By measuring the final  $m_F = 0$  spin population as a function of applied phase shift, we can map interference fringes for this type of spin-mixing interferometer. We can also change the spin-mixing duration  $t_{1,2}$  to change the number of atoms in the side modes of the interferometer and investigate the spin population in either the short-time or the long-time evolution regime.

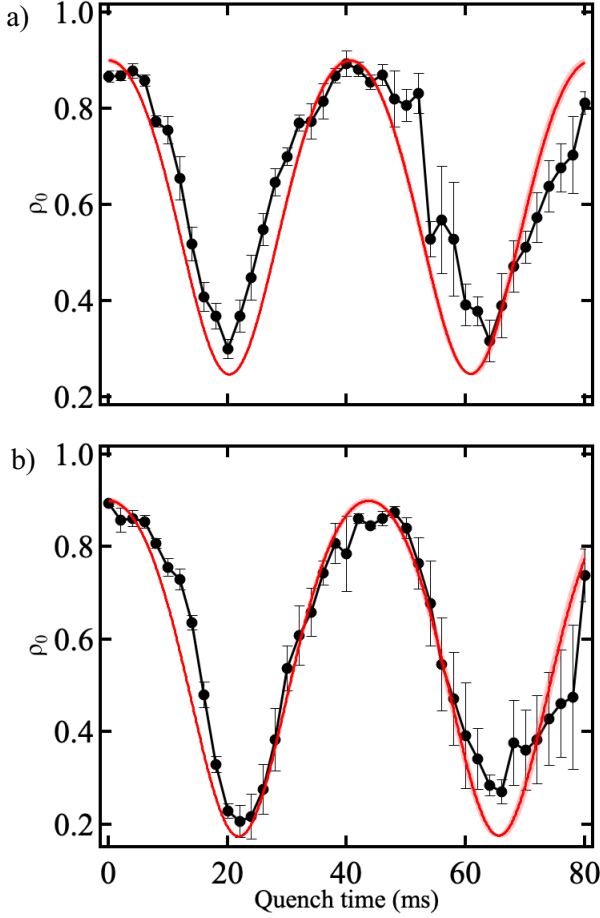


Figure 5. Measured  $m_F=0$  population fraction,  $\rho_0$ , as a function of spin evolution time after the quench. Initial states are prepared via (a) double-sided seeding and (b) single-sided seeding. The black dots and lines are experimental data. The error bars are the standard error from five experimental runs. Red lines are the truncated Wigner simulation results with q/h=-5 Hz, c/h=18.5 Hz, and N=21000. The value of q is determined from the microwave calibration. The value of N is the experimental average atom number. The value of c was adjusted as a fitting parameter within a range given by the measured fluctuations in trap frequency. The light red error bands indicate the standard deviation predicted by the truncated Wigner approximation at each time step.

# 4. Results

## 4.1. Spin-mixing Dynamics of Different Initial States

The spin-mixing dynamics for initial states that are prepared using either single-sided seeding or double-sided seeding methods with a total of 10% of atoms in the side modes  $|F=1, m_F=\pm 1\rangle$  and effective quadratic Zeeman shift q/h=-5 Hz are shown in Fig. 5a and Fig. 5b, respectively.

The black dots in Fig. 5 are the measured experimental data showing the number fraction of atoms in  $|F=1 m_F=0\rangle$  state as a function of time after quench. The error bars represent the standard

error that arises from averaging five data sets for each time. The error bars are smaller at early time and increase as the evolution time increases. The main contribution to the error bars comes from the atom number variation from one experimental realization to another, which is about 20% of the total atom number. The red lines are theoretical predictions of the spin-mixing dynamics using the truncated Wigner approximation (TWA) [23]. The simulation was done using parameters q/h = -5 Hz and a number of atoms N=21000. In this and the following, we allow c to vary within the range of a few Hz, consistent with the trap frequency fluctuations, here c/h = 18.5 Hz. The simulation time steps are set to 0.1 ms. The error bands in light red indicate the standard deviation predicted by the TWA simulation. In the simulation, we set the initial phase  $\phi = 0$ . We observe a good agreement of oscillation period and amplitude between the experiment and theory. The spin oscillations are sinusoidal. After 60 ms of spin evolution, the deviation between the experimental data and the theoretical simulation becomes larger and larger, and the error bars of the experimental data grow larger than the simulation as well. We note that the TWA simulation is an ideal theory that does not take into account any of the technical noise in the experiment such as magnetic field noise, shot-to-shot number fluctuations, atom losses from the trap, fluctuations of trap frequencies, and microwave amplitude noise.

#### 4.2. Interference Fringes

Just like with optical interferometers, interference patterns can be observed at the output of the spin-mixing interferometer. Fig. 6 shows the interference fringes of our double-sided seeding spin-mixing interferometry. In Fig. 6a to Fig. 6d, the final number fraction in the  $m_F=0$  state,  $\rho_0$ , is plotted as a function of the imprinted phase  $\Phi$  with different spin-mixing times. Fig. 6a-d show fringes for spin-mixing time of 8 ms, 10 ms, 13 ms, and 18 ms, respectively, in the states splitting and recombining steps. The pulse length of the phase imprinting step is 1 ms.

For comparison, the interference fringes for singlesided seeding spin-mixing interferometry are plotted in Fig. 7. The same parameters are used as for the double-sided case, except for the different initial state.

Black circles are the experimentally measured fractional population in  $|F=1 m_F=0\rangle$  state,  $\rho_0$ , measured at the output of the interferometer after time  $t_1 + \tau + t_2$  as a function of the imprinted phase  $\Phi$ . The error bars are standard errors from five separate measurements for each imprinted phase value. The red lines are the theoretical simulation from the truncated Wigner approximation. The light red error bands indicate the standard deviation predicted by the

TWA simulation. Here, the simulation uses parameters q/h=-5 Hz for the spin-mixing dynamics and N=21000 as the atom number. The spin-dependent interaction strength c/h=19 Hz was used to fit the data in Fig. 6 while c/h=22 Hz was used to fit the data in Fig. 7. The imprinted phase  $\Phi$  is scanned from  $2\pi\times0.2$  to  $2\pi\times2.08$  in steps of  $2\pi\times0.04$ . Experimental results agree reasonably well with the theoretical model for these parameters.

Generally, both the experimental results and the theoretical simulations in single- or doublesided seeding interferometry have an apparent fringe contrast. Moreover, the oscillations of each fringe pattern have a period of  $2\pi$ , which is expected. Specifically, in Fig. 6a and Fig. 7a, where the spin evolution time is relatively short (8 ms), both the experimental data and the TWA simulations show close-to-sinusoidal fringe patterns. For a relatively short spin evolution time, a small number of atoms are transferred to the side modes due to spinexchange collisions, and the probe states become lightly entangled. As the spin evolution time increases, the non-sinusoidal fringe patterns are more and more evident in the sub-figure (b), (c), and (d) of Fig. 6 and Fig. 7, respectively. This is because for long spin evolution time, the number of entangled pairs of atoms in  $m_F = \pm 1$  states is increased. This is the regime where bright two-mode spin-squeezed and even non-Gaussian spin-squeezed states can be generated [18]. At long evolution times, the system evolves from the undepleted pump regime to the depleted pump regime, and spin-mixing-induced non-linearity plays an important role. Non-sinusoidal interference fringes can have steep slopes, indicating some nonlinear effects that could possibly lead to metrological gain in the phase estimation. The mechanism for the metrological gain is two-mode spin squeezing generated by spin-exchange collisions [11]. Experimental data agree with the model qualitatively in all cases, but not quantitatively in all cases. We attribute the disagreement to technical noise present in the experiment, which is not captured by the simulation, such as atom loss during spin evolution, magnetic field noise and microwave amplitude noise, atom number fluctuations and trap frequency fluctuations. We also notice that the phase of the highest peak in figure (d) is shifted by  $\sim \pi$  compared to the other sub-figures in both Fig. 6 and Fig. 7. This phase difference is induced by the spin-mixing dynamics at long evolution time. Our TWA simulations for the fringes at 18 ms spin evolution time also show such a shift, however it is smaller at only  $\sim 0.8\pi$ . The TWA simulation is able to capture the interference fringe shapes qualitatively even in the non-sinusoidal cases. This agrees with our findings in Ref. [23].

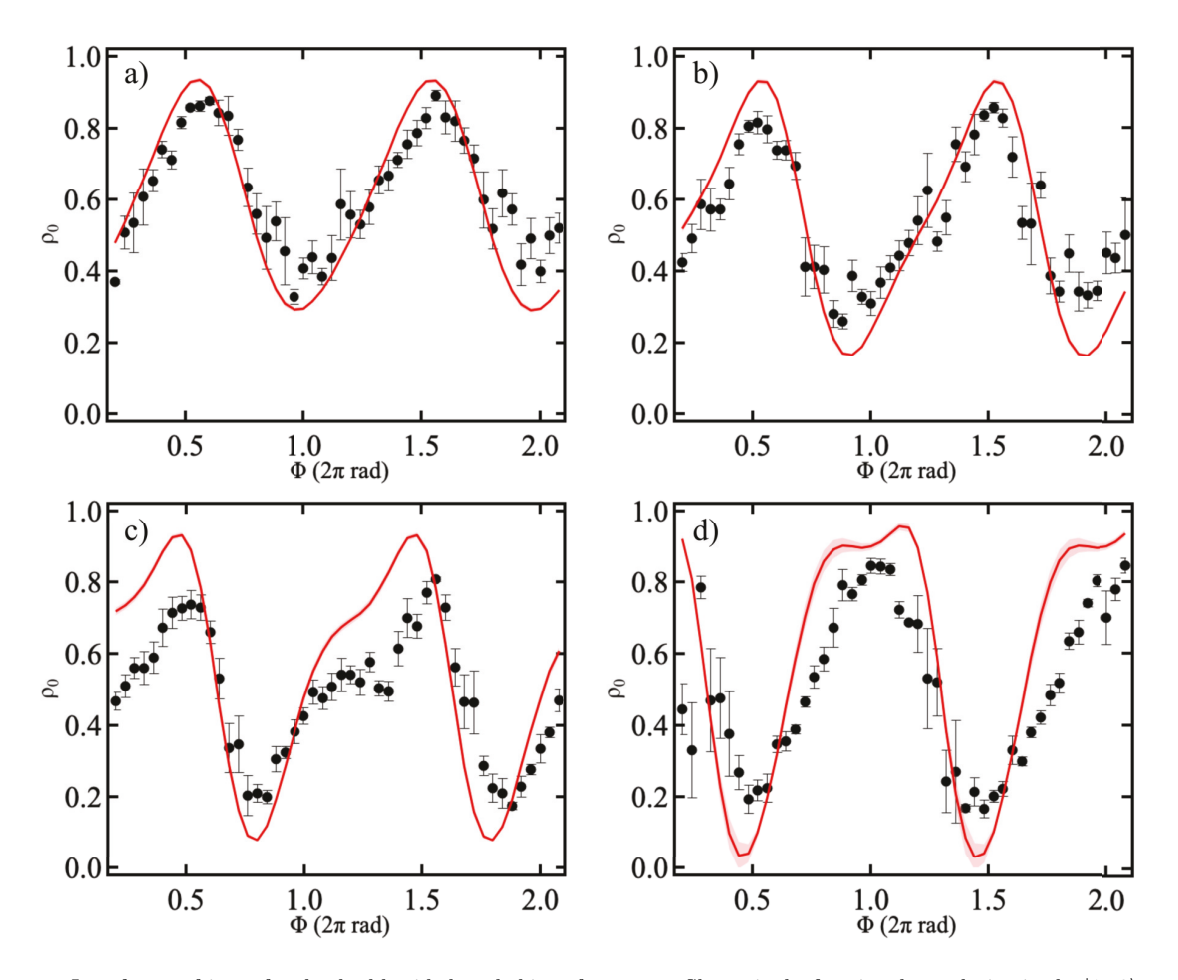


Figure 6. Interference fringes for the double-sided seeded interferometer. Shown is the fractional population in the  $|1, 0\rangle$  component,  $\rho_0$ , at the output of the interferometer (at time  $t_1 + \tau + t_2$ ) as a function of the imprinted phase  $\Phi$ . The spin-mixing time  $t_1 = t_2$  of "splitting" and "recombining" steps from (a) to (d) are 8 ms, 10 ms, 13 ms, and 18 ms, respectively. Black circles are the experimental data. Black error bars are standard errors from five separate measurements. Red lines are TWA simulation results with parameters q/h = -5 Hz, c/h = 19 Hz, and N = 21000. The red error bands depict the standard deviation predicted by the TWA simulation. The experimental data and the TWA simulation show close-to-sinusoidal fringe patterns in (a) at the short spin-mixing time of 8 ms. Interference fringes become non-sinusoidal in (b), (c), and (d) when the spin-mixing time increases, which indicates the nonlinear nature of the interferometer.

#### 4.3. Phase Sensitivity Measurement

In our experiment, the phase sensitivity of the spinmixing interferometry is obtained using the error propagation method, which is defined in Eq. 11. The average total atom number in  $|F=1, m_F=\pm 1\rangle$ states,  $\langle N_s(t) \rangle$ , and the standard deviation of  $N_s(t)$ ,  $\Delta N_s(t)$  are obtained from Stern-Gerlach absorption images of repeated runs. To calculate the phase sensitivity, we narrow the measurements to a small phase range where metrological gain is more likely to happen than in other areas, guided by the theoretical simulations. For each imprinted phase, we measure  $\langle N_s(t) \rangle$  and  $\Delta N_s(t)$  with relatively high resolution. The measurements at each imprinted phase value are repeated ten times to calculate averages and standard deviations.

Fig. 8 shows the phase sensitivity estimations

when the spin-mixing time  $t_1$  is 10 ms, and the initial state is prepared with the single-sided seeding method. In Fig. 8a and Fig. 8c, the black circles are experimental data of the total number in the  $|F=1, m_F=\pm 1\rangle$  states  $\langle N_s(t)\rangle$  as a function of imprinted phase  $\Phi$ . Each data point is averaged from ten data sets for each phase  $\Phi$ . circles in Fig. 8b and d are the standard deviation of the experimental data for  $N_s(t)$ . The red lines in Fig. 8(a-d) are guides to the eye, drawn using polynomials up to eighth order for (a,b) and Hermite interpolation up to third order in (c,d). The phase sensitivity estimation results resulting from the two different interpolation methods are shown as black lines in Fig. 8e and f, respectively. The black lines are the calculated phase sensitivity using the error propagation method normalized to the standard quantum limit. The red lines in Fig. 8e and f are the standard

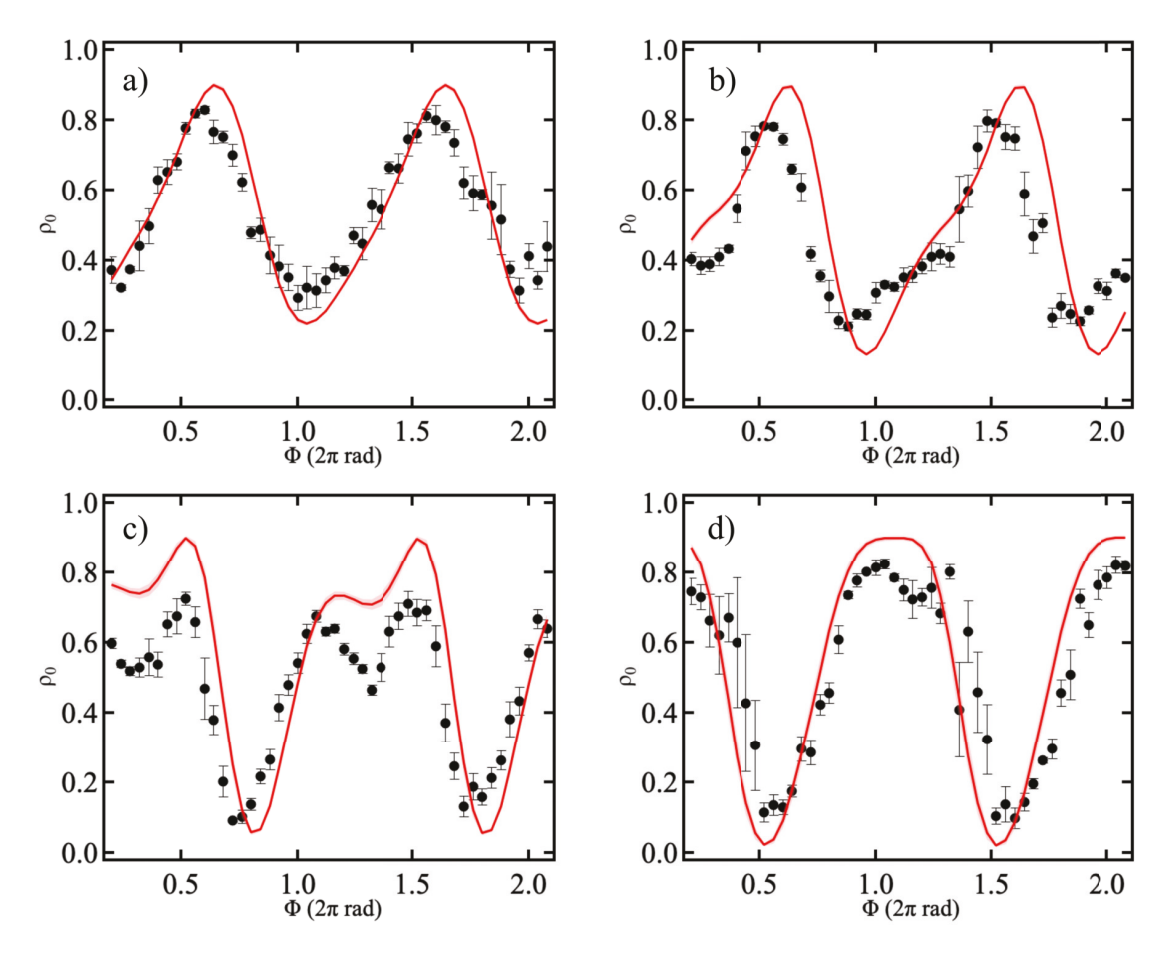


Figure 7. Interference fringes for the double-sided seeded interferometer. Shown is the fractional population in the  $|1, 0\rangle$  component,  $\rho_0$ , at the output of the interferometer (at time  $t_1 + \tau + t_2$ ) as a function of the imprinted phase  $\Phi$ . The spin-mixing time  $t_1 = t_2$  of "splitting" and "recombining" steps from (a) to (d) are 8 ms, 10 ms, 13 ms, and 18 ms, respectively. Black circles are the experimental data. Black error bars are standard errors from five separate measurements. Red lines are TWA simulation results with parameters q/h = -5 Hz, c/h = 22 Hz, and N = 21000. The red error bands depict the standard deviation predicted by the TWA simulation. The experimental data and the TWA simulation show close-to-sinusoidal fringe patterns in (a) at the short spin-mixing time of 8 ms. Interference fringes become non-sinusoidal in (b), (c), and (d) when the spin-mixing time increases, which indicates the nonlinear nature of the interference ter. The single-sided seeding interferometer performs similarly to the one with double-sided seeding in terms of the interference patterns.

quantum limit normalized to unity, for comparison. The SQL here is defined as  $\Delta\Phi_{\rm SQL}=1/\sqrt{\langle N_s(t_1)\rangle}$ , where  $\langle N_s(t_1)\rangle$  is the mean value of the total atom number in  $|F=1,\ m_F=\pm 1\rangle$  states right after the "splitting" step, and  $t_1=10$  ms. Here, we measured  $N_s(t_1)$  30 times, and the red error band on top of the SQL indicates the statistical uncertainty that arises from averaging 30 data points measured at  $t_1$ . Compared with the SQL (red line), the black lines below the SQL from  $\Phi=2\pi\times 1.52$  to  $\Phi=2\pi\times 1.56$  indicates a metrological gain in phase sensitivity. For comparison, we also draw the quantum Cramér-Rao bound of the probe states as blue dashed lines and the Heisenberg sensitivity limit as green dash-dotted lines, all normalized to the SQL.

The standard quantum limit is derived by assuming the atoms  $N_s(t_1)$  in the probe states are

separable. Therefore the lowest achievable sensitivity for atoms in separable states is bounded by the quantum Cramér-Rao bound, which is equivalent to the SQL. However, in our experiment, the atoms  $N_s(t_1)$  are forming spin-mixing induced probe states with correlations generated between each pair of atoms in the  $|F=1, m_F=\pm 1\rangle$  states. The quantum Cramér-Rao bound of the correlated states is then supposed to give a better sensitivity than the SQL. The results in Fig. 8e and f show that with the same atom number,  $N_s(t_1)$ , prepared in the separable probe states and the correlated probe states, the phase sensitivity of the correlated states (black line) induced by the spin-mixing dynamics can overcome the SQL (red line) and achieve metrological gain compared to its classical reference. Here, due to the long evolution time, we attribute the metrological gain to the combination of

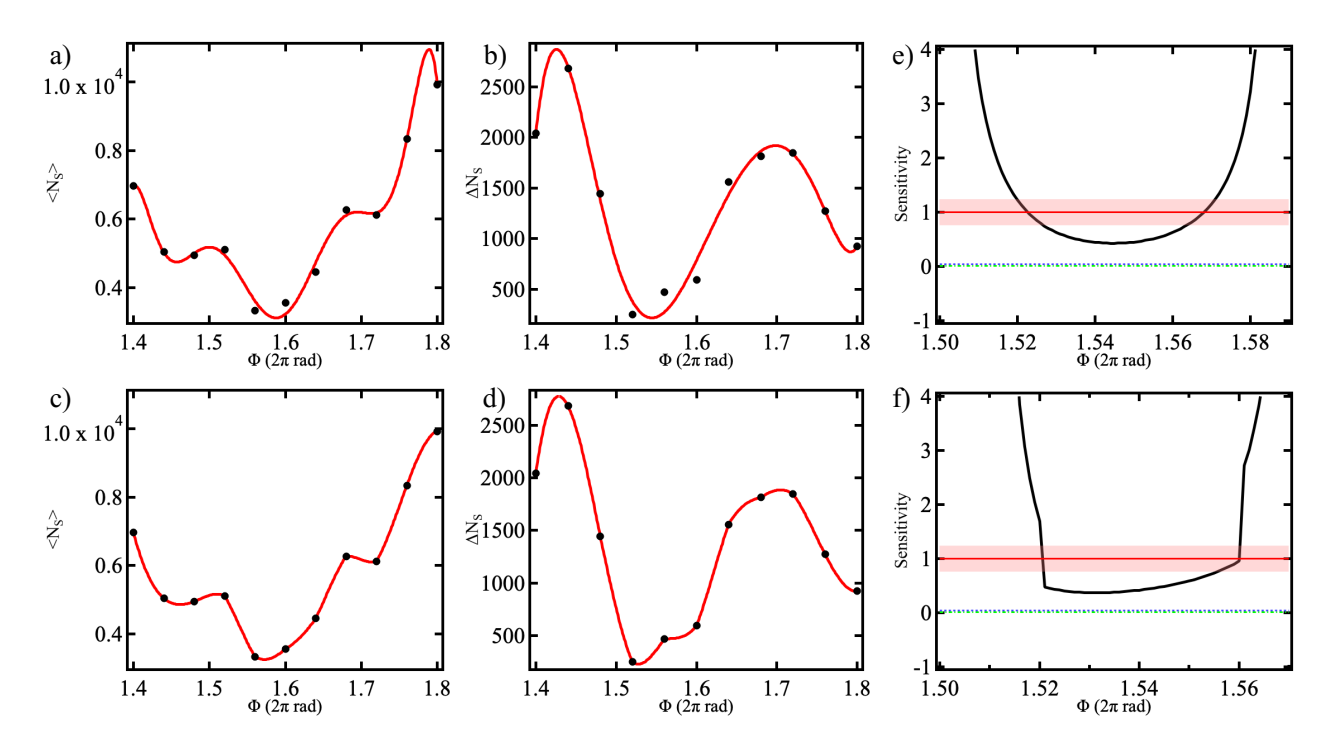


Figure 8. Phase sensitivity measurement using error propagation method. Black circles in (a) and (c) are experimental mean values of the total number in the  $|F=1, m_F=\pm 1\rangle$  states as a function of phase. Each point is an average of ten data. Black circles in (b) and (d) are the standard deviation of the experimental data. The red lines in (a-d) are guides to the eye, drawn as polynomials of order eight for (a,b) and Hermite functions of order three for (c,d). Black lines in (e) are the phase sensitivity estimation using the interpolation from (a) and (b). Black lines in (f) are the phase sensitivity using the interpolation from (c) and (d), respectively. Results are normalized to the SQL. The red lines in (c) and (d) are the normalized SQL defined as  $1/\sqrt{\langle N_s(t_1) \rangle}$  where  $t_1=10$  ms. Red bands are the standard deviation that arises from averaging 30 data points measured at  $t_1$ . Blue dash lines are the quantum Cramér-Rao bound of the probe states, and green dash and dot lines are the Heisenberg sensitivity limit.

nonlinear effects that distort the interference fringes, as well as the pair-correlations generated by spin-mixing.

We now further explore the phase sensitivity using experiments with different spin-mixing times as well as single- and dual-sided seeded initial states. Figure 9a to 9c show the phase sensitivity of single-sided seeding atom interferometers at  $t_1$  equal to 10 ms, 13 ms, and 18 ms, respectively. The black lines are the phase sensitivity calculated from the experimental data using the error propagation method and normalized to the standard quantum limit. The red lines are standard quantum limits normalized to unity. The light red error band indicates the statistical uncertainty of the SQL that arises from averaging 30 data points measured at the end of the first spin-mixing time  $t_1$ . For comparison, we draw the quantum Cramér-Rao bound of the probe states as blue dashed lines and the Heisenberg sensitivity limit as green dash-dotted lines, all normalized to the SQL. Fig. 9d to 9f show the phase sensitivities in black lines in terms of the metrological gain obtained with  $t_1$  equal to 10 ms, 13 ms, and 18 ms, respectively, with the shaded regions indicating uncertainties. At  $t_1 = 10$  ms, the experimental error propagation data (black line) decrease below the SQL (red line) from  $\Phi \approx 2\pi \times 1.52$  to  $\Phi \approx 2\pi \times 1.57$ .

The maximum gain is found at  $\Phi = 2\pi \times 1.54$  with G = 3.69 dB where the metrological gain is defined as  $G = 10 \log_{10}(\Delta \Phi_{\rm SQL}/\Delta \Phi)$ . For comparison, the black dashed line is the TWA simulated error propagation data, for which the maximum gain is obtained at  $\Phi = 2\pi \times 1.58$  with G = 5.25 dB, which is  $\sim 1.6$  dB greater than the experimental result. At  $t_1 = 13$  ms, the experimental gain is G = 1.96 dB at  $\Phi = 2\pi \times 1.5$ , and the TWA simulated gain is G = 3.44 dB at  $\Phi =$  $2\pi \times 1.56$ . Both theoretical and experimental data show that the metrological advantage of the interferometry is weaker at  $t_1 = 13$  ms than  $t_1 = 10$  ms. In Fig. 9c, the minimum of the experimental data is about four times above the SQL, and the theoretical simulation is very close to the SQL, indicating no metrological gain is obtained when  $t_1 = 18 \text{ ms.}$ 

Fig. 10 shows the phase sensitivity of double-sided seeding interferometers. We use the same method to obtain the error propagation data, TWA simulation data, Cramér-Rao bound, and the Heisenberg sensitivity limit as in Fig. 9 with the same legends. Figure 10a to 10c show the phase sensitivities obtained with  $t_1$  equals to 8 ms, 13 ms, and 18 ms, respectively. Fig. 10d to 10f show the corresponding phase sensitivities in terms of the metrological gain. At  $t_1 = 8$  ms,

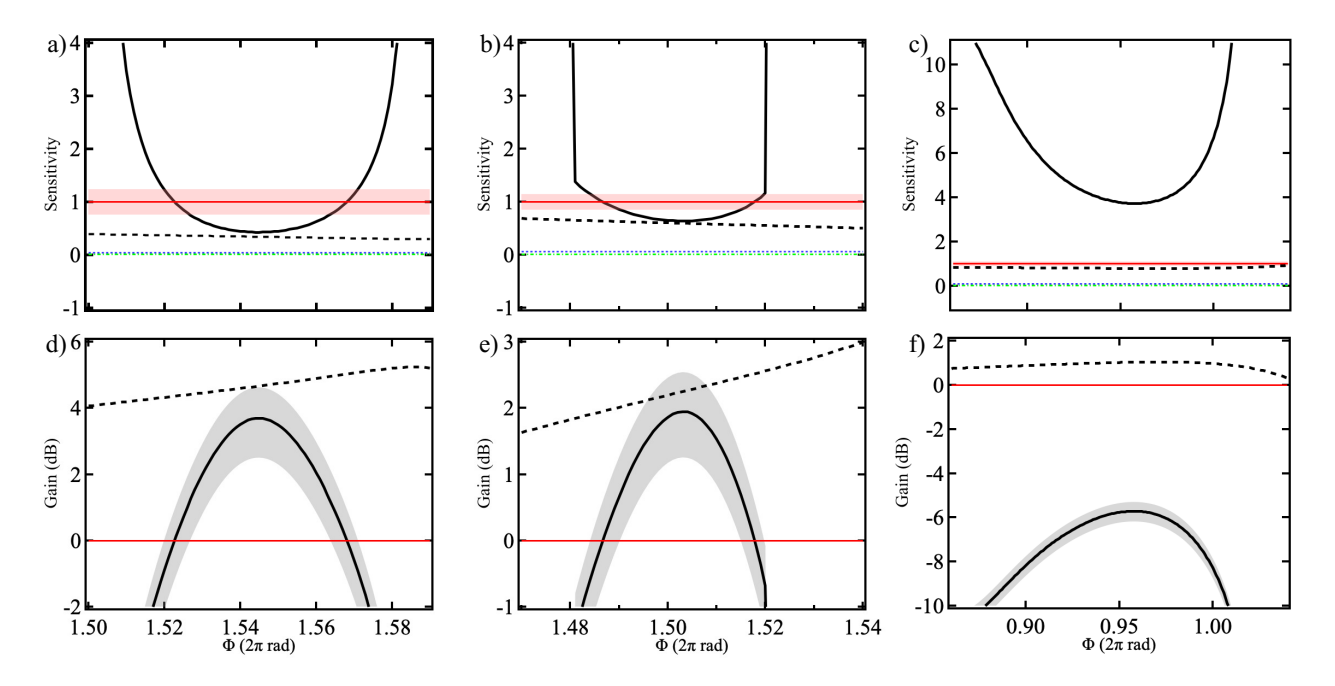


Figure 9. Phase sensitivities of single-sided seeded spin-mixing interferometers with the spin-mixing time,  $t_1$ , of (a) 10 ms, (b) 13 ms, and (c) 18 ms. Figures (d) to (f) are the corresponding plots in terms of the metrological gain. When  $t_1=10$  ms, the maximum metrological gain is obtained at  $\Phi=2\pi\times1.54$  with G=3.69 dB. Dashed black lines are the phase sensitivities calculated from the TWA simulated data, with a gain of 5.25 dB at  $\Phi=2\pi\times1.58$ . The gain becomes smaller at  $t_1=13$  ms, and there is no gain at  $t_1=18$  ms.

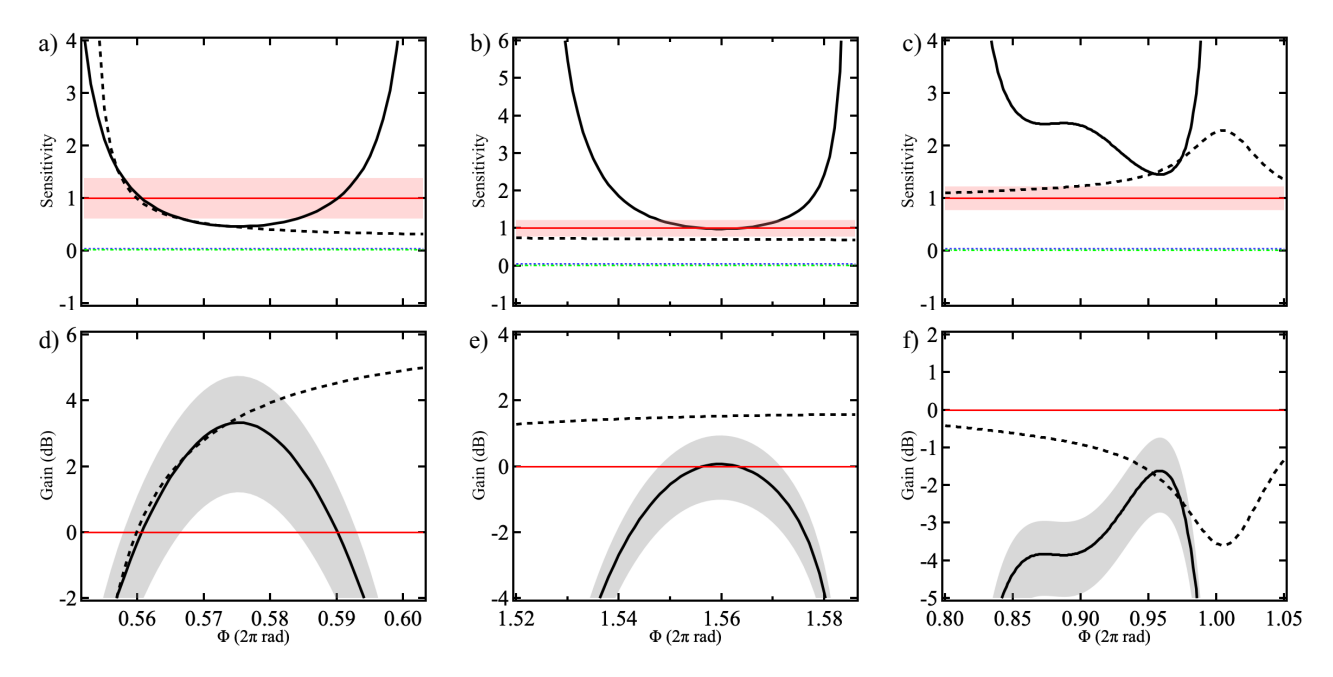


Figure 10. Phase sensitivities of double-sided seeding atom interferometers with the spin-mixing time,  $t_1$ , of (a) 8 ms, (b) 13 ms, and (c) 18 ms. Figures (d) to (f) are the corresponding plots in terms of the metrological gain. When  $t_1 = 8$  ms, the maximum metrological gain is obtained at  $\Phi = 2\pi \times 0.573$  with G = 3.33 dB indicates a metrological gain. Dashed black lines are the phase sensitivities calculated from the TWA simulated data, with a gain of 5.53 dB at  $\Phi = 2\pi \times 0.66$ . The gain becomes barely visible at  $t_1 = 13$  ms, and no gain at  $t_1 = 18$  ms.

the experimental error propagation data (black line) decreases below the SQL (red line) from  $\Phi \approx 2\pi \times 0.56$ to  $\Phi \approx 2\pi \times 0.59$ . The maximum gain is found at  $\Phi = 2\pi \times 0.573$  with G = 3.33 dB. For comparison, the TWA simulated error propagation shown as black dashed line has the maximum gain at  $\Phi = 2\pi \times 0.66$ with G = 5.53 dB. In Fig. 10b, where  $t_1 = 13$  ms, the experimental error propagation data are within the error band of the SQL, indicating little or no metrological enhancement for this evolution time. The TWA simulated error propagation data is closer to the SQL than that in Fig. 10a, showing that the simulated advantage of the interferometry is also weaker at  $t_1 = 13$  ms compared to  $t_1 = 8$  ms. In Fig. 10c, experimental data are above the SQL, indicating no metrological gain is obtained when  $t_1 = 18$  ms.

One could expect that longer mixing time would always lead to more entanglement and therefore a larger gain in sensitivity. However, since the spin populations are oscillating in time (see Fig. 5), the spin-squeezing will also oscillate in time. In other words, we are in a regime beyond the undepleted pump approximation, and, in this regime, entanglement does not grow forever. We think that this is the reason why longer evolution time does not always yield better sensitivity. We found similar results in our calculations [23]. In order to experimentally verify that this is the reason for the observed reduced sensitivity at longer evolution time, one would need to do a full tomography of the states and determine the entanglement entropy, which is beyond the scope of this paper.

We observe similar gains for both single-sided seeding and double-sided seeding. In our numerical calculations, we also found similar gains for both single and double-sided seeding [23]. Although the gains are similar, the experimental requirements to implement single- or double-sided seeding can be chosen differently, based on the capabilities of an apparatus. Double-sided seeding can be achieved with an RF rotation at kHz frequencies, while single-sided seeding requires a sequence of microwave pulses at GHz frequencies.

It must be pointed out that the discrepancies between the experimental data and the TWA simulations are still somewhat large in both Fig. 9 and Fig. 10. It might be explained from two different perspectives: (1) From the theoretical point of view, with 10% of initial seeding, after several milliseconds of spin-mixing dynamics, lots of atoms are coupled from  $|F=1,m_F=0\rangle$  state to  $|F=1,m_F=\pm 1\rangle$  states. The system is in a deeply entangled regime where the undepleted pump approximation cannot capture the dynamics of the system very well [28]. Therefore, only a full quantum calculation might describe the system well enough [23].

(2) From the experimental point of view, shot-to-shot atom number fluctuations, atom loss during a single experimental cycle, fluctuations of microwave amplitude, and fluctuations of trap frequencies can be expected to cause the realistic spin-mixing interferometer to exhibit a significant deviation the ideal theoretical simulation.

Our experimental phase sensitivity data suggest that spin-mixing interferometry with seeded states and intermediate evolution times can beat the standard quantum limit. The seeding can be important for future quantum technologies because it speeds up the creation of entangled pairs in the system. The resulting larger populations in the arms of the interferometer make detection easier in the experiments.

#### 5. Summary

We demonstrated experimental spin-mixing interferometry with microwave-dressed F=1 antiferromagnetic sodium spinor BECs. Contrary to previous work, our interferometer operates with seeded initial states and in the regime of intermediate to long evolution time. We analyzed the metrological enhancement which suggests gain of up to 3.69 dB beyond the standard quantum limit for certain operating parameters and evolution times, starting with 10% seeded initial states. Our experiment is currently limited by technical noise such as shot-to-shot number fluctuations, magnetic field and microwave fluctuations, trap frequency fluctuations, and atom loss from the trap.

There are several things that could be done in the future to further improve the interferometry performance at a longer spin evolution time. Since the error propagation method relies on calculating the derivative of the atom number in  $|F=1, m_F=\pm 1\rangle$  states with respect to the imprinted phase, we can increase the data resolution by narrowing the step size. This will increase the accuracy of data interpolation and could improve the error propagation results. Another option is to acquire a much larger data set which would allow post-selection on atom numbers to narrow the uncertainties due to shot-to-shot atom number fluctuations.

While our system is more of a prototyping platform that requires two 5 by 10 feet large optical tables, it can be imagined that spinor BEC systems might eventually be miniaturized more and more and could become real quantum technological devices, such as quantum-enhanced magnetic field or microwave sensors with high spatial resolution and metrological gain. By extending spin-mixing interferometry to the domain of seeded initial states, our work improves the understanding of the possible parameter regimes at which such future devices could be operated.

# 6. Acknowledgements

Acknowledgements: We gratefully acknowledge support from AFOSR Grant No. FA9550-20-1-0071 and from the National Science Foundation through Grant No. PHY-1846965.

- Cheiney P, Fouché L, Templier S, Napolitano F, Battelier B, Bouyer P and Barrett B 2018 Phys. Rev. Applied 10(3) 034030
- [2] Geiger R, Ménoret V, Stern G, Zahzam N, Cheinet P, Battelier B, Villing A, Moron F, Lours M, Bidel Y, Bresson A, Landragin A and Bouyer P 2011 Nature Communications 2 474
- [3] Stray B, Lamb A, Kaushik A, Vovrosh J, Rodgers A, Winch J, Hayati F, Boddice D, Stabrawa A, Niggebaum A, Langlois M, Lien Y, Lellouch S, Roshanmanesh S, Ridley K, de Villiers G, Brown G, Cross T, Tuckwell G, Faramarzi A, Metje N, Bongs K and Holynski M 2022 Nature 602 590-594
- [4] Pitkin M, Reid S, Rowan S and Hough J 2011 Living Reviews in Relativity 14 5
- [5] Barrett B, Condon G, Chichet L, Antoni-Micollier L, Arguel R, Rabault M, Pelluet C, Jarlaud V, Landragin A, Bouyer P and Battelier B 2022 AVS Quantum Science 4 014401
- [6] Jaffe M, Haslinger P, Xu V, Hamilton P, Upadhye A, Elder B, Khoury J and Müller H 2017 Nature Physics 13 938– 942
- [7] Giovannetti V, Lloyd S and Maccone L 2006 Phys. Rev. Lett. 96(1) 010401
- [8] Caves C M 1981 Phys. Rev. D 23(8) 1693–1708
- [9] Kitagawa M and Ueda M 1993 Phys. Rev. A 47(6) 5138– 5143
- [10] Jie J, Guan Q and Blume D 2019 Phys. Rev. A 100(4) 043606
- [11] Pezzè L, Smerzi A, Oberthaler M K, Schmied R and Treutlein P 2018 Rev. Mod. Phys. 90(3) 035005
- [12] Bollinger J J, Itano W M, Wineland D J and Heinzen D J 1996 Phys. Rev. A 54(6) R4649–R4652
- [13] Lee H, Kok P and Dowling J P 2002 Journal of Modern Optics 49 2325–2338
- [14] Yurke B, McCall S L and Klauder J R 1986 Phys. Rev. A 33(6) 4033–4054
- [15] Zhang Z and Duan L 2013 Phys. Rev. Lett. 111(18) 180401
- [16] Wrubel J P, Schwettmann A, Fahey D P, Glassman Z, Pechkis H K, Griffin P F, Barnett R, Tiesinga E and Lett P D 2018 Phys. Rev. A 98(2) 023620
- [17] Linnemann D, Strobel H, Muessel W, Schulz J, Lewis-Swan R J, Kheruntsyan K V and Oberthaler M K 2016 Phys. Rev. Lett. 117(1) 013001
- [18] Liu Q, Wu L, Cao J, Mao T, Li X, Guo S, Tey M and You L 2022 Nature Physics 18 167–171
- [19] Widera A, Gerbier F, Fölling S, Gericke T, Mandel O, and Bloch I 2006 New Journal of Physics 8 152
- [20] Gross C, Zibold T, Nicklas E, Estève J and Oberthaler M K 2010 Nature  ${\bf 464}$  1165–1169
- [21] Slusher R E, Hollberg L W, Yurke B, Mertz J C and Valley J F 1985 Phys. Rev. Lett. 55(22) 2409–2412
- [22] Boyer V, Marino A M, Pooser R C and Lett P D 2008 Science 321(5888) 544–547
- [23] Zhang Q and Schwettmann A 2019 Phys. Rev. A 100(6) 063637
- [24] Yi S, Müstecaphoğlu O E, Sun C P and You L 2002 Phys. Rev. A 66(1) 011601
- [25] Law C K, Pu H and Bigelow N P 1998 Phys. Rev. Lett. 81(24) 5257–5261
- [26] Zhao L, Jiang J, Tang T, Webb M and Liu Y 2014 Phys. Rev. A 89(2) 023608

- [27] Leslie S R A 2008 On spinor condensates as amplifiers, sensors and tunable quantum playgrounds for studies of spin Ph.D. thesis University of California, Berkeley
- [28] Gabbrielli M, Pezzè L and Smerzi A 2015 Phys. Rev. Lett. 115(16) 163002
- [29] Morgenstern I, Zhong S, Zhang Q, Baker L, Norris J, Tran B and Schwettmann A 2020 Review of Scientific Instruments 91 023202